



# *In situ* Synthesis of Au-Induced Hierarchical Nanofibers/Nanoflakes Structured BiFeO<sub>3</sub> Homojunction Photocatalyst With Enhanced Photocatalytic Activity

Yan'an Li<sup>1</sup>, Jiao Li<sup>1\*</sup>, Long Chen<sup>1\*</sup>, Haibin Sun<sup>1</sup>, Hua Zhang<sup>1</sup>, Hong Guo<sup>2</sup> and Liu Feng<sup>2</sup>

<sup>1</sup> School of Materials Science and Engineering, Shandong University of Technology, Zibo, China, <sup>2</sup> Analysis & Testing Center, Shandong University of Technology, Zibo, China

## OPEN ACCESS

### Edited by:

Yuxin Zhang,  
Chongqing University, China

### Reviewed by:

Dong Guohui,  
Shaanxi University of Science and  
Technology, China  
Xiaoying Liu,  
Chongqing Technology and Business  
University, China

### \*Correspondence:

Jiao Li  
haiyan9943@163.com  
Long Chen  
lchen830@sdut.edu.cn

### Specialty section:

This article was submitted to  
Catalysis and Photocatalysis,  
a section of the journal  
Frontiers in Chemistry

Received: 03 September 2018

Accepted: 12 December 2018

Published: 04 January 2019

### Citation:

Li Y, Li J, Chen L, Sun H, Zhang H,  
Guo H and Feng L (2019) *In situ*  
Synthesis of Au-Induced Hierarchical  
Nanofibers/Nanoflakes Structured  
BiFeO<sub>3</sub> Homojunction Photocatalyst  
With Enhanced Photocatalytic Activity.  
Front. Chem. 6:649.  
doi: 10.3389/fchem.2018.00649

In order to further improve the photocatalytic performance of BiFeO<sub>3</sub> (BFO), novel Au-induced hierarchical nanofibers/nanoflakes structured BiFeO<sub>3</sub> homojunctions (Au<sub>x</sub>-BFO,  $x = 0, 0.6, 1.2, 1.8, 2.4$  wt%) were *in situ* synthesized through a simple reduction method with assist of sodium citrate under the analogous hydrothermal environment. The effect of loading amount of Au nanoparticles (NPs) on the physicochemical properties and photocatalytic activity was investigated in detail. The Au<sub>1.2</sub>-BFO NFs sample show the best photocatalytic activity (85.76%), much higher than that for pure BFO samples (49.49%), mainly due to the hierarchical nanofibers/nanoflakes structured homojunction, the surface plasmon resonance (SPR) effect of Au NPs, as well as the presence of defects (Fe<sup>2+</sup>/Fe<sup>3+</sup> pairs and oxygen vacancy). Furthermore, the possible formation mechanism of the unique homojunction and the enhanced photocatalytic mechanism for the degradation of methylene blue (MB) dye are proposed. It is proven that holes (h<sup>+</sup>) play the decisive role in the photocatalytic process. The present work provides a fascinating way to synthesize efficient homojunctions for the degradation of organic pollutants.

**Keywords:** bismuth ferrite, homojunction, SPR effect, defects, photodegradation

## INTRODUCTION

Nowadays, energy crisis and environmental deterioration issues are severely detrimental for economic development and human health (Wang et al., 2013). Semiconductor photocatalysis as an efficient and green technology can convert solar energy into chemical energy to dispose of these issues (Wang et al., 2013; Wang H. et al., 2017). In order to fully exploit the solar energy, it is necessary to explore visible light responsive photocatalysts with excellent photocatalytic activities (Zhang et al., 2017).

Among the variety of visible-light-driven semiconductor materials, BiFeO<sub>3</sub> (BFO) has attracted a great deal of attention due to its narrow band gap (2.2~2.5 eV), good chemical stability and low cost (Wang et al., 2013; Niu et al., 2015). In addition, the room temperature multiferroic property makes it easily recovered from the treated water to avoid the secondary pollution (Zhang et al., 2017). However, the rapid recombination rate of photogenerated electron-hole pairs and low quantum yield limit its practical application (Huo et al., 2011; Srivastav and Gajbhiye, 2012; Niu et al., 2015). Therefore, much efforts have been made to improve its photocatalytic performance, such as element doping (Wang et al., 2012; Ahmada et al., 2017; Irfan et al., 2017; Yang et al., 2018),

morphology control (Mohan and Subramanian, 2013; Zhang Q. et al., 2016), noble metal deposition (Li S. et al., 2013; Zhang et al., 2015), and semiconductor coupling (Li Z. et al., 2013; Humayun et al., 2016).

Compared to that of bulk materials, the reduced radial dimension and the extremely large surface-to-volume ratio of one-dimension (1D) nanofibrous structure can promote the rapid transfer of photogenerated charge carriers to the surface, and thus enhance the separation efficiency (Li S. et al., 2013). Furthermore, the perpendicular transport direction of photogenerated electrons and holes can further effectively inhibit the recombination of photogenerated electron-hole pairs (Mohan and Subramanian, 2013). Therefore, the synthesis of BFO sample with nanofibrous structure is in favor of enhancing the photocatalytic activity.

Noble metal (e.g., Ag, Au, Pt, etc.) deposition is also an efficient way to enhance the photocatalytic activity (Li et al., 2015; Niu et al., 2015; Zhang et al., 2015). Among them, Au nanoparticles (NPs) exhibit excellent a chemical stability and a characteristic absorption peak in the visible wavelength range due to the strong surface plasmon resonance (SPR) effect (Li S. et al., 2013; Li et al., 2015). The deposited Au NPs can not only act as electron-trapping centers to reduce the recombination rate of photogenerated electron-hole pairs, but also can act as light harvesters enhancing the light absorbing ability and as catalytic sites for the photocatalytic reaction (Lin et al., 2017; Chiu et al., 2018). Significantly, the formed Schottky junctions between Au NPs and BFO nanofibers (NFs) can adjust the interfacial band structure and thus promote the separation and transfer of photogenerated charge carriers.

In comparison with heterojunction built with different semiconductors. Besides the band alignment of two semiconductors, the creation of heterojunctions is also dependent on other properties of semiconductor, such as electron affinity and work function (Ye et al., 2017). The homojunction is constructed by the same semiconductor materials with different crystal phases, exposing facets or semiconductor types, etc., which can avoid the disadvantages of heterojunction fabrication (Huang et al., 2017). The enhanced photocatalytic activity of heterojunctions or homojunctions is mainly dependent on the space charge accumulation or depletion at the interfaces of two phases (Ye et al., 2017). The homojunction structure can also introduce an internal field to effectively facilitate surface charge separation, retard the recombination of photogenerated carriers, and thus remarkably improve the photocatalytic performance. However, there are few reports on the fabrication of BFO homojunction, especially for the aspect of *in situ* synthesis.

In this work, an distinctive Au NPs deposited BFO homojunction, in which BFO nanoflakes are assembled on the surface of BFO NFs, was *in situ* synthesized through a simple reduction method under the analogous hydrothermal environment. The effect of loading amount of Au NPs on the physicochemical properties and photocatalytic activity was investigated in detail. Furthermore, it proposed a possible formation mechanism of the unique homojunction and the enhanced photocatalytic mechanism for the degradation of

methylene blue (MB) dye over Au<sub>x</sub>-BFO NFs under simulated solar light irradiation.

## EXPERIMENTAL

### Preparation of Au<sub>x</sub>-BFO NFs

BFO NFs (Au<sub>x</sub>-BFO NFs,  $x = 0$  wt%) were prepared *via* a sol-gel method combined with an electrospinning technique. All the chemical reagents used for the synthesis were analytical grade. Bismuth nitrate (Bi(NO<sub>3</sub>)<sub>3</sub>·5H<sub>2</sub>O) and ferric nitrate (Fe(NO<sub>3</sub>)<sub>3</sub>·9H<sub>2</sub>O) with the Bi: Fe molar ratio of 1.11:1 (to make up for the loss of Bi ions during the calcination process) were dispersed in methylglycol by ultrasonic to form a homogeneous solution. Then the viscosity and pH value of the solution were adjusted by 2.5 mL of glacial acetic acid, called solution A. g of poly(vinylpyrrolidone) (PVP,  $M_w = 1,300,000$ ) was added to the mixed solvent of N,N-dimethylformamide (DMF) and ethanol with the volume ratio of 2:1, called solution B. Solution B was added dropwise to solution A with constantly stirring for 24 h to form the pre-spinning solution which has a pH of 2.0. The pre-spinning solution was loaded into a plastic syringe connected with a stainless needle and then fixed onto the electrospinning system. An optimized high voltage of 15 kV was applied to the needle with the flow rate of 0.4 mL/h. The distance was 20 cm from the needle to the rotating drum collector. The as-spun NFs were dried at 60°C for 4 h, calcined at 350°C for 30 min with a heating rate of 2°C/min, and then calcined at 600°C for 120 min with a heating rate of 5°C/min in air.

Au NPs deposited BFO NFs (Au<sub>x</sub>-BFO NFs,  $x = 0.6, 1.2, 1.8, 2.4$  wt%) were synthesized by a simple reduction method with sodium citrate. In a typical procedure, 57.38 mg of BFO NFs were first dispersed in 50 mL of deionized water, followed by adding a certain amount of HAuCl<sub>4</sub> (3 mmol/L) and sodium citrate (0.04 mol/L). Then the suspension was kept stirring at 150°C for 30 min in oil bath. After cooled to room temperature naturally, the obtained products were centrifuged, washed with deionized water and absolute ethanol for several times, and then dried at 80°C for 24 h. The loading amount of Au NPs on BFO NFs were 0.6, 1.2, 1.8, and 2.4 wt% (mass ratio of Au to BFO), which were defined as Au<sub>0.6</sub>-BFO NFs, Au<sub>1.2</sub>-BFO NFs, Au<sub>1.8</sub>-BFO NFs, and Au<sub>2.4</sub>-BFO NFs, respectively.

### Characterization

The phase structures were identified by X-ray diffraction (XRD; D8 Advance, Bruker AXS, German) with Cu K $\alpha$  radiation ( $\lambda = 1.5418$  Å) at 40 kV and 50 mA in a  $2\theta$  ranging from 20 to 70°. The morphologies were observed by field emission scanning electron microscope (FE-SEM; Sirion 200, FEI, USA). The transmission electron microscopy (TEM) and high resolution TEM (HRTEM) were performed at a field emission transmission electron microscope (TEM; Tecnai G2 F20 S-TWIN, FEI, USA) with an accelerating voltage of 200 kV. UV-vis diffuse reflectance spectra (DRS) were measured at room temperature by UV-Vis spectrometer (UV-Vis; UV-3600plus, Shimadzu, Japan) with the wavelength range of 350–800 nm using BaSO<sub>4</sub> as a reflectance. The measurements of magnetic properties were carried out by a superconducting quantum interference device magnetometer

(FM, MPMS XL-7, Qunatum Design, USA). The element chemical states were characterized by X-ray photoelectron spectrometer (XPS; PHI-5300, PHI, USA) with an Al K $\alpha$  X-ray radiation. The photoluminescence (PL) spectra were measured on the fluorescence spectrophotometer (PL; Hitachi F-4600, Hitachi, Japan) with the excitation wavelength of 230 nm and a 150 W xenon lamp as the light source.

## Photocatalytic Activity Evaluation

Twenty five milligram of Au<sub>x</sub>-BFO NFs were added to 30 mL of 10 mg/L MB solution with ultrasound for 10 min. After stirring in the dark for 30 min to reach the adsorption-desorption equilibrium, the suspension system was exposed to simulated solar light irradiation (CHF-XM-500W xenon lamp, Beijing Perfectlight Company, China). During the photocatalytic reaction process, the suspension was taken out at every 30 min interval and centrifuged to remove the photocatalyst. The MB concentration was measured by a UV-vis spectrophotometer at the wavelength of 666 nm.

## RESULTS AND DISCUSSION

### XRD Analysis

The XRD patterns of Au<sub>x</sub>-BFO NFs ( $x = 0, 0.6, 1.2, 1.8, 2.4$  wt%) are shown in **Figure 1**. All the diffraction peaks of pure BFO NFs can be indexed to the rhombohedral perovskite structure with  $R3m$  space group of the BiFeO<sub>3</sub> phase (JCPDS card no. 86-1518) (Chen et al., 2017). The strong diffraction peaks also imply the good crystallinity. In addition, the crystalline structures of BFO NFs are not changed after depositing Au NPs.

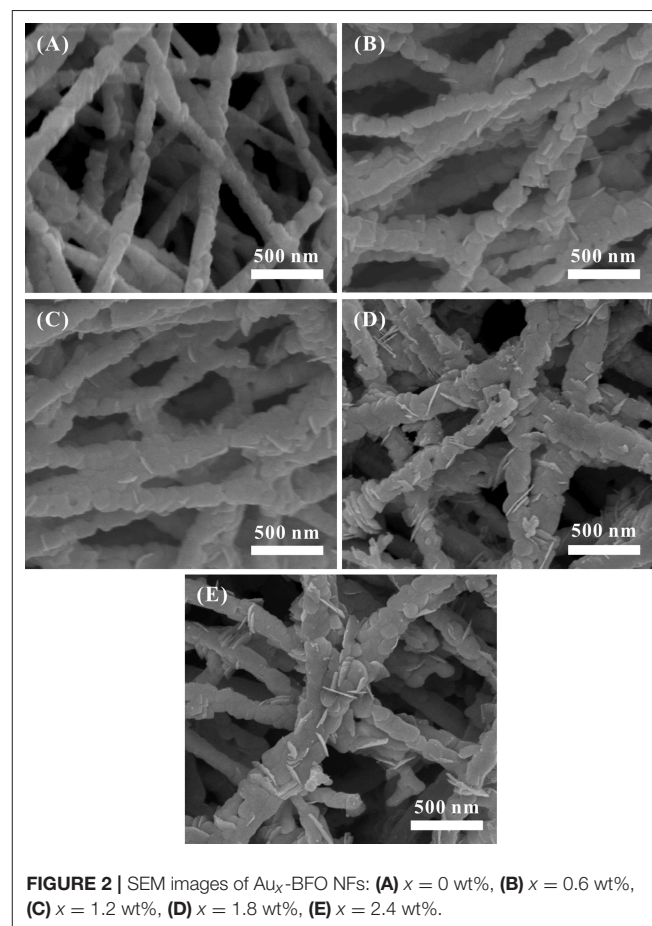
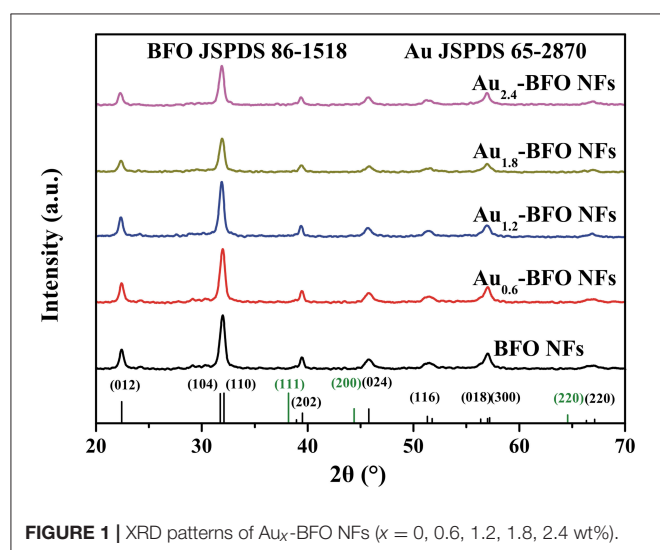
### Microstructures

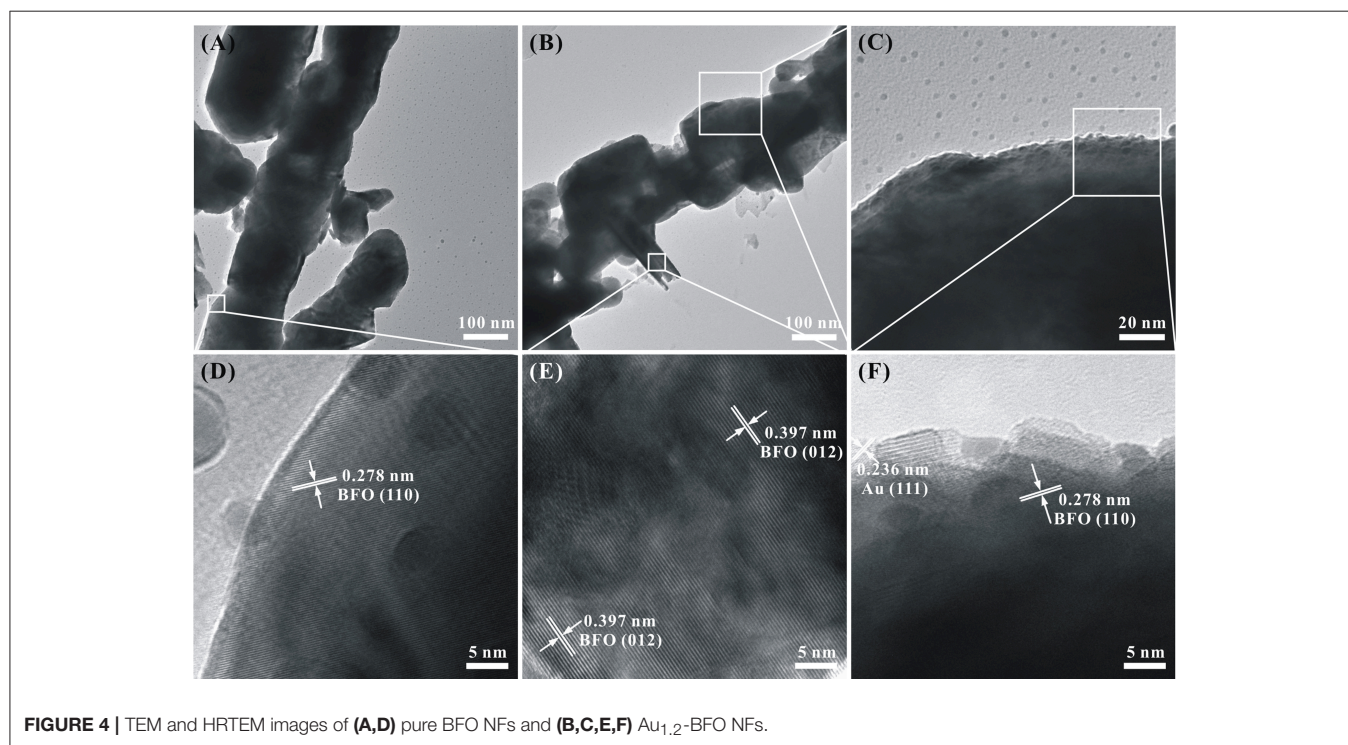
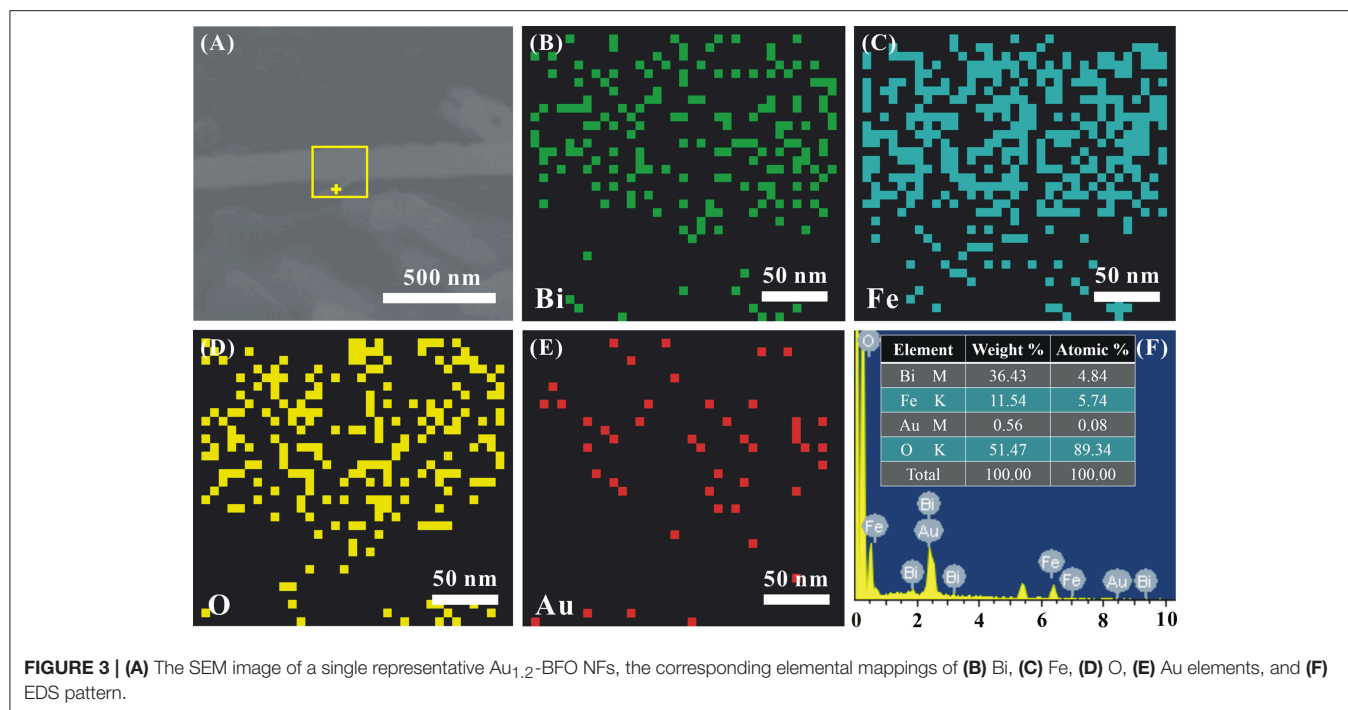
**Figure 2** shows the SEM images of Au<sub>x</sub>-BFO NFs ( $x = 0, 0.6, 1.2, 1.8, 2.4$  wt%). It can be seen from **Figure 2A** that the pure BFO NFs exhibit a uniform nanofibrous structure with compactly packed and continuous nanoparticles. The diameter of BFO NFs is about 100–200 nm. As shown in **Figures 2B–E**, there is no

obvious change of the nanofibrous structure for BFO NFs with Au NPs deposition, but some thin nanoflakes are embedded in the surface of nanofibers, and the number of nanoflakes increases with the increase of the loading amount of Au NPs.

The EDS mapping is performed to clarify the chemical composition and element distribution in Au<sub>1.2</sub>-BFO NFs, as shown in **Figure 3**. It can be clearly seen that Bi, Fe, and O elements are uniformly distributed throughout the single nanofiber (**Figures 3A–D**). Au NPs are dispersed well on BFO NFs, instead of agglomerating together (**Figure 3E**). More importantly, The EDS result (**Figure 3F**) recorded at the “+” position in **Figure 3A** shows that the main elements of the nanoflake are Bi, Fe, Au, and O. It is worthy to note that the atomic ratio of Bi/Fe is almost 1:1, nearly corresponding to the composition of BFO. The trace amount of Au shows that Au NPs are also deposited on the nanoflake.

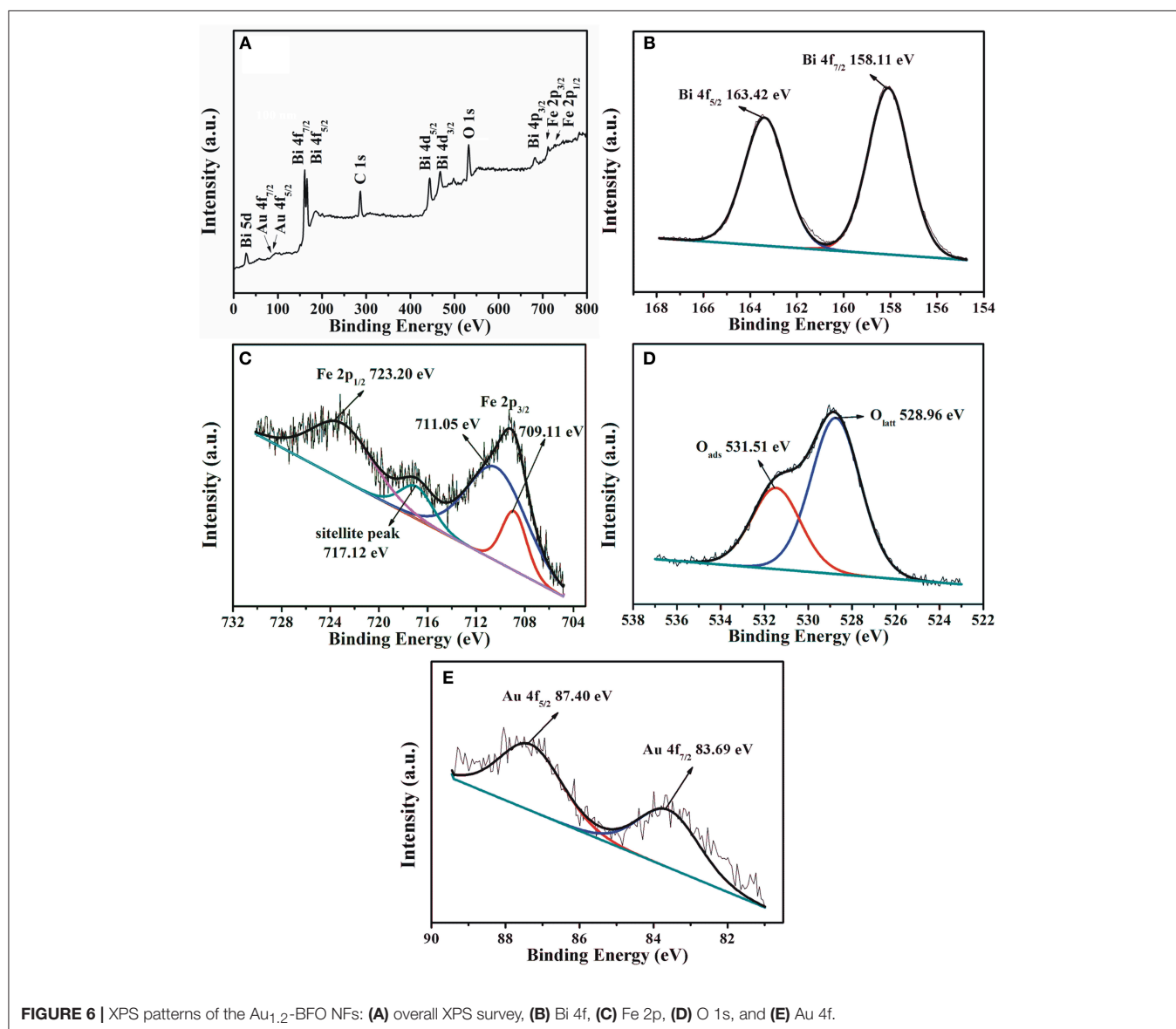
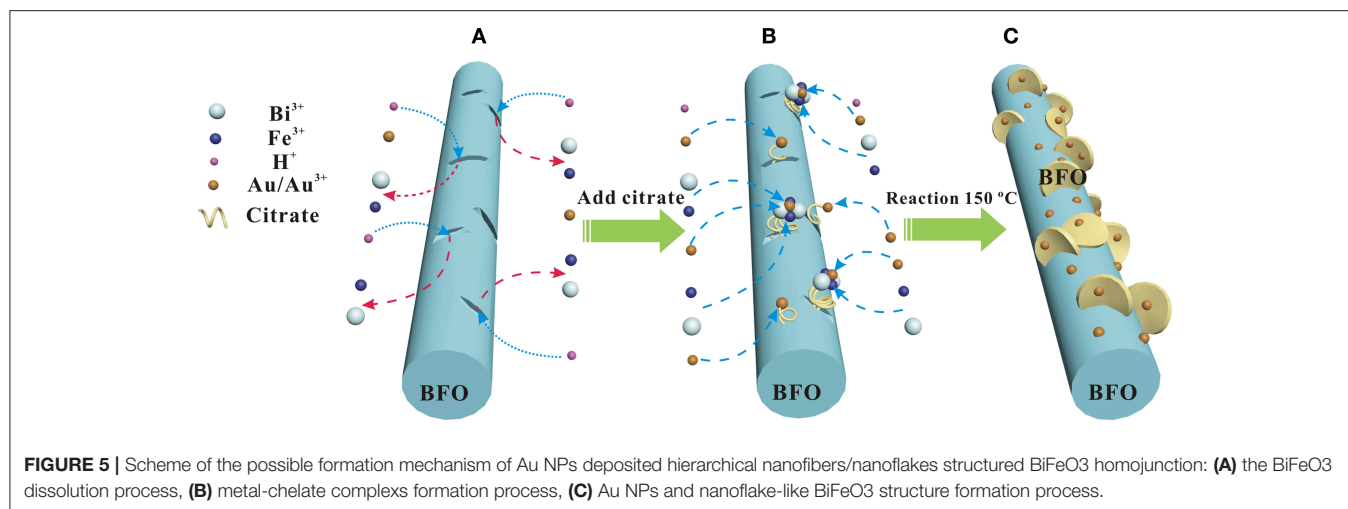
In order to further illustrate the morphology and microstructure of pure BFO NFs and Au<sub>1.2</sub>-BFO NFs, TEM technology is used. As shown in **Figure 4A**, the pure BFO sample is nanofibrous structure compactly packed with nanoparticles. The HRTEM image in **Figure 4D** is collected from the square area in **Figure 4A**. The interplanar spacing of 0.278 nm corresponds to the (110) lattice plane of the rhombohedral perovskite BFO structure. **Figure 4B** shows the TEM image





of Au<sub>1.2</sub>-BFO NFs. It can be seen that the morphology is still the nanofibrous structure. However, the surface of the nanofiber becomes rougher and the composed nanoparticles appear to be more prominent after depositing the Au NPs on the surface of BFO NFs. Furthermore, new nanoflake-like structures are formed and embedded in the BFO NFs. In order

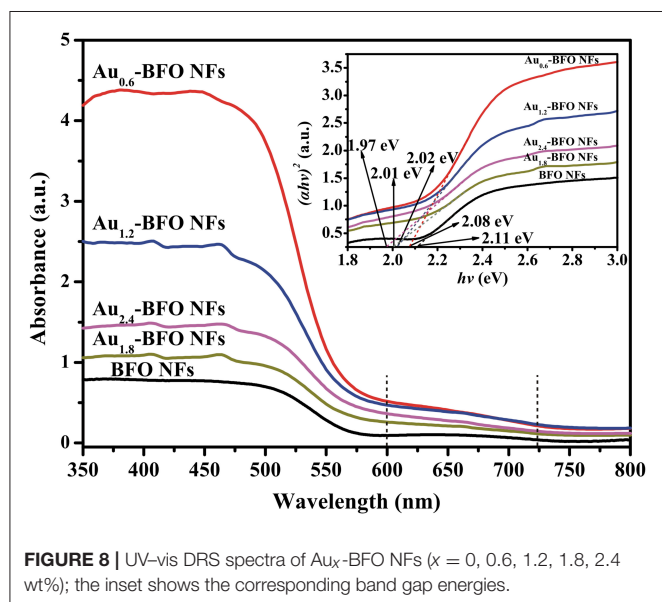
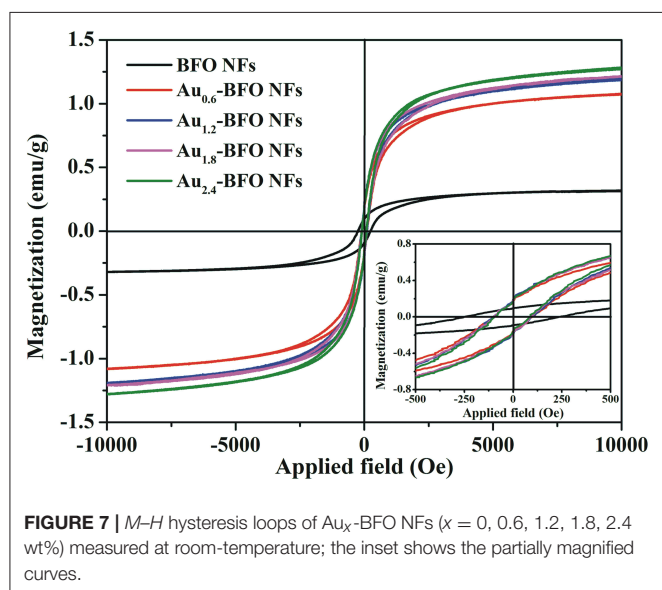
to confirm the structure of nanoflakes, the HRTEM is used, and the result of which is shown in **Figure 4E**. The interplanar spacing of 0.397 nm is ascribed to the (012) lattice plane of the rhombohedral perovskite BFO structure, further implying that the new formed nanoflake-like structure is indeed BFO phase. Therefore, homojunctions will be formed between BFO NFs



and BFO nanoflakes. From **Figure 4B**, there is no obvious Au NPs deposited on the BFO surface. In order to clearly observe the deposited Au NPs, the magnified TEM image is shown in **Figure 4C**. It can be seen that Au NPs with the size of about 5 nm are indeed deposited uniformly on the BFO surface. The according HRTEM image is shown in **Figure 4F**. The interplanar spacing of 0.236 nm matches well with the (111) lattice plane of the cubic Au structure (Wang P. et al., 2017).

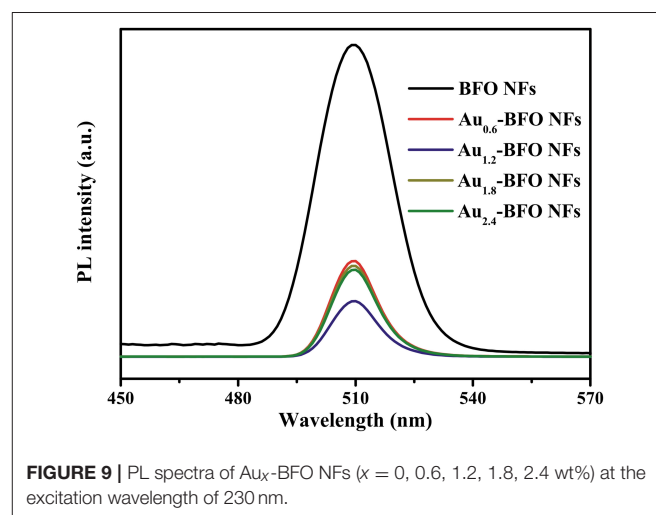
The possible formation mechanism of the Au NPs deposited hierarchical nanofibers/nanoflakes structured BFO homojunction is proposed in **Figure 5**. Firstly, the HAuCl<sub>4</sub> is decomposed to AuCl<sub>3</sub> and HCl in the aqueous solution. BiFeO<sub>3</sub>, being regarded as the product of a combination of Bi<sub>2</sub>O<sub>3</sub> and Fe<sub>2</sub>O<sub>3</sub>, is soluble in the weak acidic environment (Sakar et al.,

2013). Therefore, the generated HCl can decompose the BiFeO<sub>3</sub> to generate Bi<sup>3+</sup> and Fe<sup>3+</sup> ions in the solution (**Figure 5A**). In particular, the decomposition reaction prefers to occur at the defects on the surface of BFO NFs where the higher surface energy have. The defects may be generated during the oxidation decomposition of organic material (PVP) under the high calcination temperature. Secondly, the citrate present in the solution can act as a chelating agent to react with Bi<sup>3+</sup>, Fe<sup>3+</sup>, and Au<sup>3+</sup> ions to form stable metal-chelate complexes (**Figure 5B**). In addition, due to the presence of defects, the citrate can anchor on the surface of BFO NFs (Mudunkotuwa and Grassian, 2010). Finally, the uniform Au NPs and nanoflake-like BFO structure are formed on the surface of BFO NFs under the effect of the citric acid in the analogous hydrothermal environment (**Figure 5C**). With the increase of the HAuCl<sub>4</sub> content (the increase of the loading amount of Au NPs), more Bi<sup>3+</sup> and Fe<sup>3+</sup> ions pass from the defects on the surface of BFO NFs to the solution, and more nanoflake-like BFO structure are formed.



## XPS Analysis

The chemical state and elemental composition of Au<sub>1.2</sub>-BFO NFs are analyzed by XPS technology. According to the overall XPS survey (**Figure 6A**), only Bi, Fe, O, Au, and C elements can be detected in the sample. The peak of C 1s located at 284.5 eV is used for calibration (Dou et al., 2015; Chen et al., 2016). As shown in **Figure 6B**, the two peaks centered at around 158.11 eV and 163.42 eV can be assigned to the binding energy of Bi 4f<sub>7/2</sub> and Bi 4f<sub>5/2</sub>, respectively. It is confirmed that the bismuth species in Au<sub>1.2</sub>-BFO NFs is the oxidation state of +3. From the high resolution XPS spectra of Fe 2p in **Figure 6C**, the three peaks located at 710.79, 717.12, and 723.20 eV can be ascribed to the Fe 2p<sub>3/2</sub>, satellite, and Fe 2p<sub>1/2</sub> peaks, respectively. In addition, the Fe 2p<sub>3/2</sub> peak can be fitted into two peaks located at 711.05 and 709.11 eV, which are attributed to Fe<sup>3+</sup> and Fe<sup>2+</sup> species, respectively (Wu et al., 2016). The presence of Fe<sup>2+</sup> species may come from the reduction of Fe<sup>3+</sup> species by citric acid under high temperature environment. In order to meet



the requirement of charge equilibrium, oxygen vacancy should be formed accompanied by the Fe<sup>2+</sup> species. The O 1s curve in **Figure 6D** can be splitted into two peaks with Lorentzian-Gaussian function. The peaks at 531.51 and 528.96 eV can be ascribed to the surface adsorbed oxygen (O<sub>ads</sub>) and lattice oxygen (O<sub>latt</sub>) species, respectively (Bharathkumar et al., 2016; Chen et al., 2016). The O<sub>ads</sub> species may originate from the -OH groups bonded to the metal cations in the oxygen deficient region (Guo et al., 2016; Sun et al., 2017), which can be converted to oxygen-related free radicals to participate in the photocatalytic reaction. Moreover, the more O<sub>ads</sub> species usually mean the more oxygen vacancies it possesses, and also the better photocatalytic activity. From **Figure 6E**, the binding energies of 83.69 eV and 87.40 eV are ascribed to the Au 4f<sub>7/2</sub> and Au 4f<sub>5/2</sub> peaks, respectively, indicating that the gold is present in the form of metallic gold (Au<sup>0</sup>) in the Au<sub>x</sub>-BFO NFs. This can be ascribed to the reduction by citric acid under high temperature environment. Therefore, the metallic gold have been successfully deposited on the surface of BFO NFs. Whereas, the binding energies of Au 4f in the Au<sub>1,2</sub>-BFO NFs are 0.3 eV below the standard binding energy of a metallic gold foil (Jovic et al., 2013), indicating the existence of electron transfer from BFO NFs to Au NPs for the different Fermi levels (Li S. et al., 2013). In addition, the loading amount of Au NPs is measured to be 1.14%, almost equal to the theoretical value of 1.2%.

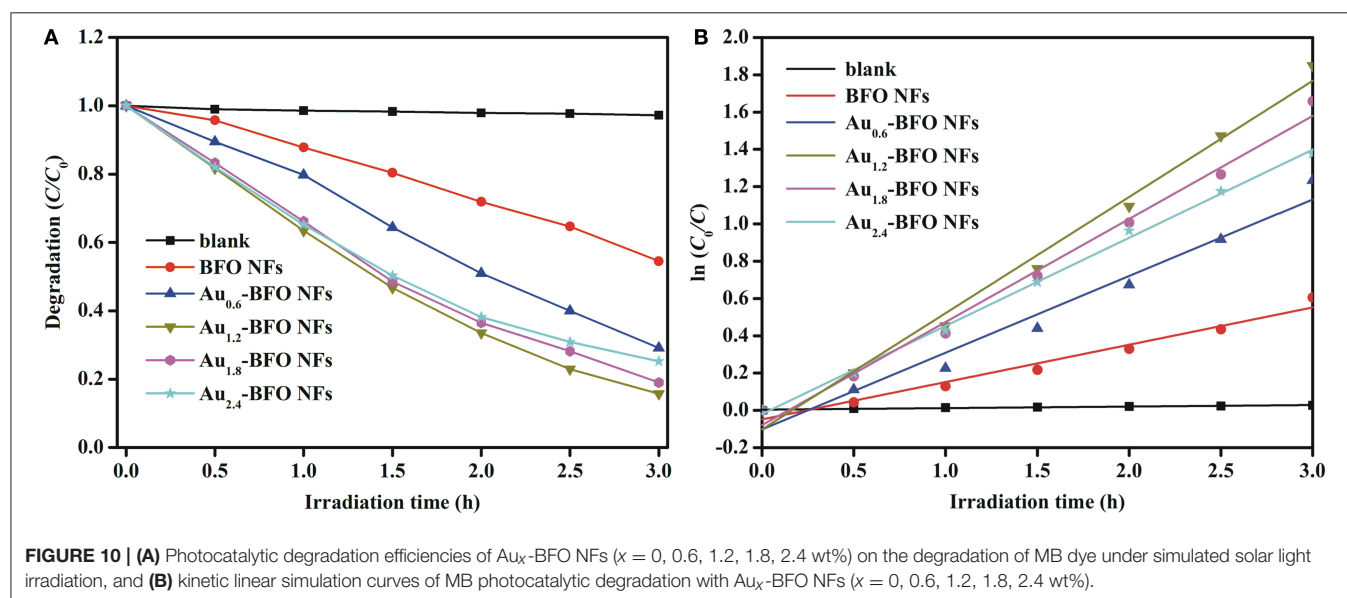
## Ferromagnetism Analysis

In order to investigate the effect of Au on the magnetic property of Au<sub>x</sub>-BFO NFs, the room-temperature magnetic hysteresis (*M-H*) loops are shown in **Figure 7**. It can be seen that all BFO NFs exhibit the weak-ferromagnetic (FM) characters, which is due to the suppressed cycloidal spin structure and the coexistence of Fe<sup>3+</sup> and Fe<sup>2+</sup>, thereby resulting in the FM spins in the system (Xu et al., 2014; Modak et al., 2016). The pure BFO NFs show the saturation magnetization (*M<sub>s</sub>*) value of 0.32 emu/g.

When Au NPs are deposited on the surface of BFO NFs, the *M<sub>s</sub>* value is enhanced with the increase in the loading amount of Au NPs. The *M<sub>s</sub>* values are 1.07, 1.19, 1.22, and 1.27 emu/g for BFO NFs with the loading amount of Au NPs of *x* = 0.6, 1.2, 1.8, and 2.4 wt%, respectively. The gradually enhanced magnetic properties of Au<sub>x</sub>-BFO NFs could be attributed to the new formed nanoflake-like structures, where the confined dimensions (15 nm) facilitate the enhancement of FM properties (Chauhan et al., 2012). In addition, the rather large magnetic moment of Au NPs explains the enhanced magnetic properties with increase in loading amount of Au NPs (Nealon et al., 2012). From the inset of **Figure 7**, an obvious off-center displacement in magnetic field axis is shown in the *M-H* curves. This can be ascribed to the exchange bias (EB) effect of antiferromagnet (AFM) - FM ordering in BFO NFs, where the AFM-core/FM-shell-like structure can be formed in the well-defined 1D structure (Sakar et al., 2016). Compared to that of the pure BFO NFs, the off-center displacement of Au<sub>x</sub>-BFO NFs is relatively less pronounced, which is ascribed to the enhanced FM spins caused by the emergence of nanoflake-like structures.

## Optical Properties

**Figure 8** shows the UV-vis DRS spectra of Au<sub>x</sub>-BFO NFs (*x* = 0, 0.6, 1.2, 1.8, 2.4 wt%) samples. It can be seen that the pure BFO NFs exhibit excellent absorption in both UV and visible light region. The absorption edge located at 575 nm is due to the bandgap transition. When the Au NPs are deposited on the surface of BFO NFs, the optical properties are obviously enhanced. In addition, the Au<sub>x</sub>-BFO NFs exhibit a weak absorption peak in the range of 600~725 nm, which are attributed to the SPR effect of Au NPs (Villa et al., 2016; Wang P. et al., 2017). The enhanced absorption in visible light is in favor of boosting the photocatalytic activity. Moreover, the band gap energies can be calculated from the plots of the ( $\alpha h\nu$ )<sup>2</sup> vs. the photon energy (*hν*) (Xu et al., 2015; Singh et al., 2018), the



results of which are shown in the inset of **Figure 8**. The band gap energies are calculated to be 2.11, 2.08, 2.02, 2.01, and 1.97 eV for the  $x = 0, 0.6, 1.2, 1.8, 2.4$  wt%, respectively. It is obvious that the band gap energies decrease slightly with the increase in the loading amount of Au NPs. The possible reason is that the deposited Au NPs can produce some lower energy levels due to the formed Schottky junction at the interface between Au NPs and BFO NFs (Papadas et al., 2015).

## PL Analysis

Photoluminescence (PL) spectra are extensively used to study the transfer and separation of photogenerated electron-hole pairs in the semiconductor material. The peak intensity can reflect the capture, migration and transfer efficiency of photogenerated electron-hole pairs. The lower PL intensity usually means the lower recombination rate of photogenerated electron-hole pairs, and also the higher photocatalytic activity (Tang et al., 2018). It can be seen from **Figure 9** that the PL intensity decreases obviously once the Au NPs are loaded on the surface of BFO NFs. Significantly, the PL intensity of Au<sub>1.2</sub>-BFO NFs is the lowest. This indicates that the deposition of Au NPs on the surface of BFO NFs can efficiently inhibit the recombination of photogenerated charge carriers, which may be attributed to that the Schottky junction formed between Au NPs and BFO NFs can efficiently promote electron transfer from BFO NFs to Au NPs, and thus decreased the recombination rate of photogenerated charge carriers (Li S. et al., 2013). However, the PL intensity increases when the loading amount of Au NPs is too much. This can be ascribed to the fact that the excess amount of Au NPs can result in an increase of surface defects, which can act as recombination centers for photogenerated charge carriers, thus leading to the increase in the recombination rate. Therefore, it is necessary to deposit an appropriate amount of Au NPs on the surface of BFO NFs to promote the efficient separation of photogenerated electron-hole pairs, thus enhancing the photocatalytic activity.

## Photocatalytic Activities

**Figure 10A** shows the photocatalytic degradation efficiencies of Au<sub>x</sub>-BFO NFs ( $x = 0, 0.6, 1.2, 1.8, 2.4$  wt%) on the degradation of MB dye under simulated solar light irradiation. For contrast, the blank experiment without any photocatalyst is carried out under the same conditions. The result shows that the MB dye is hardly degraded under simulated solar light irradiation. The degradation efficiency is only 2.77% after irradiation of 3 h. When the pure BFO sample is added to the reaction system, the degradation efficiency reaches to be 49.49% after irradiation of 3 h. However, the photocatalytic activity is still relatively poor. Once Au NPs are deposited on the surface of BFO NFs, the photocatalytic activities of Au<sub>x</sub>-BFO NFs are obviously enhanced. The enhanced activities can be ascribed to the hierarchical nanofibers/nanoflakes structured homojunction, the SPR effect of Au NPs, as well as the presence of defects (Fe<sup>2+</sup>/Fe<sup>3+</sup> pairs and oxygen vacancy). In addition, the photocatalytic activity is increased and then suppressed with the increase in the loading amount of Au NPs. When the loading amount of Au NPs is 1.2%, the photocatalytic activity is the best with the photocatalytic efficiency of 85.76% after irradiation of 3 h.

To evaluate the reaction kinetics of the degradation of MB, the plot of  $\ln(C_0/C)$  vs. time is plotted in **Figure 10B**, which shows the kinetics of the degradation process by the five photocatalysts which follow Langmuir-Hinshelwood pseudo first-order kinetic equation,  $\ln(C_0/C) = kt$ , where  $t$  is the irradiation time and  $k$  is the rate constant (Niu et al., 2015). The observed calculated rate constants  $k$  in the presence of blank sample, Au<sub>x</sub>-BFO NFs ( $x = 0, 0.6, 1.2, 1.8, 2.4$  wt%) are  $8.28 \times 10^{-3}$ ,  $200.23 \times 10^{-3}$ ,  $411.46 \times 10^{-3}$ ,  $623.27 \times 10^{-3}$ ,  $552.85 \times 10^{-3}$ , and  $472.69 \times 10^{-3} \text{ h}^{-1}$ , respectively. which also indicates that the Au<sub>1.2</sub>-BFO NFs sample exhibits the strongest photocatalytic activity among the Au<sub>x</sub>-BFO NFs ( $x = 0, 0.6, 1.8, 2.4$  wt%) samples.

In order to evaluate the stability of photocatalysts, the recycle experiment is carried out. After each recycle, the photocatalysts

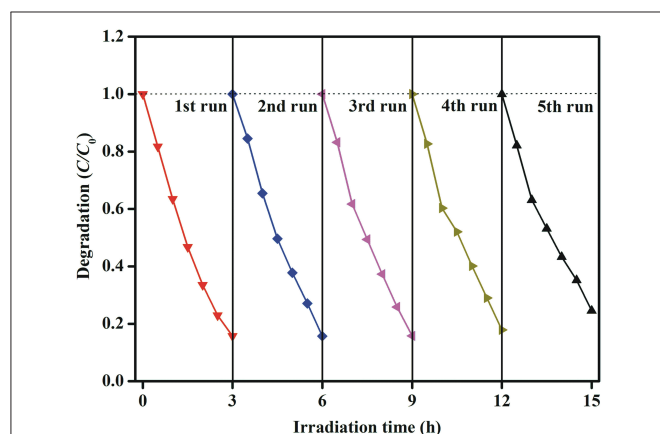


**FIGURE 11** | Stability evaluation for the photocatalytic degradation of MB dye in the presence of Au<sub>1.2</sub>-BFO NFs under simulated solar light irradiation.

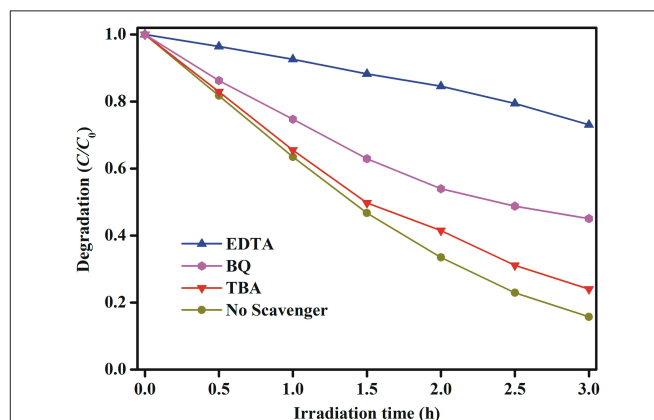


**FIGURE 12** | Active species trapping experiments of photocatalytic degradation of MB dye over the Au<sub>1.2</sub>-BFO NFs under simulated solar light irradiation with the addition of EDTA, TBA, and BQ quenchers.

are collected by simple filtration and washed with deionized water and absolute ethanol. As shown in **Figure 11**, there is no obvious loss in photocatalytic activity after five recycle test, indicating that Au<sub>x</sub>-BFO NFs photocatalysts have good stability during the photocatalytic degradation of MB dye under simulated solar light irradiation.

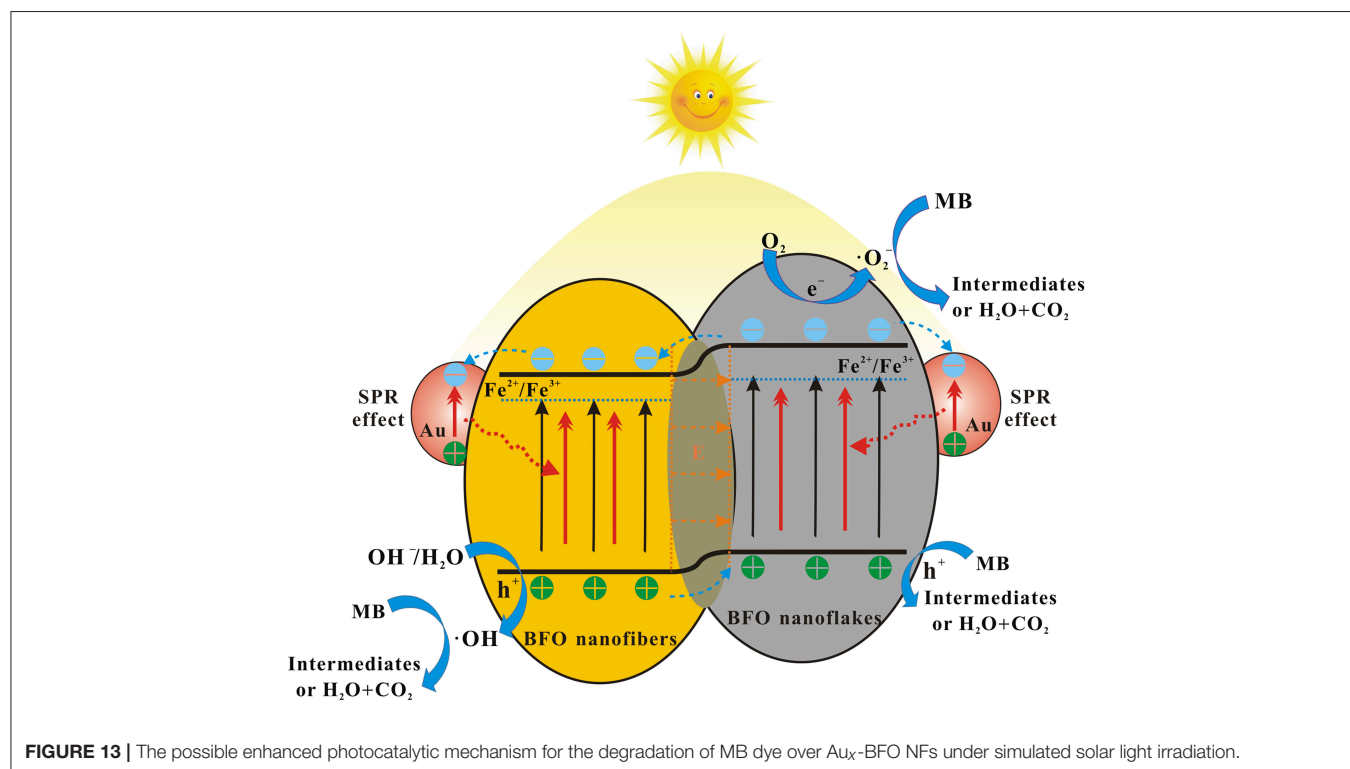
In order to explore the possible reaction pathways during the photocatalytic degradation of MB dye under simulated solar light irradiation, the trapping experiments are used to determine the main active species in this reaction system. Ethylenediaminetetraacetic acid (EDTA), tertbutyl alcohol (TBA) and benzoquinone (BQ) are used as scavengers for holes (h<sup>+</sup>), hydroxyl radicals (•OH), and superoxide radicals (•O<sub>2</sub><sup>-</sup>), respectively (Chen et al., 2016; Qiao et al., 2017; Ji et al., 2018). As can be seen from **Figure 12**, when the TBA or BQ is added, a slight reduction in MB degradation efficiency is occurred in comparison to the initial activity without addition of any scavengers, which means that •O<sub>2</sub><sup>-</sup> and •OH radicals are not the main active species. However, the photocatalytic activity is severely suppressed when EDTA is added to the reaction system, implying that photogenerated holes are the main active species and play the decisive role in the photocatalytic activity.

## Photocatalytic Mechanism

On the basis of the aforementioned experimental and active species trapping results, the possible enhanced photocatalytic mechanism is illustrated in **Figure 13**. It can be ascribed to the following aspects: (1) Nanofibers/nanoflakes structured homojunction. It is well-known that nanoflakes with ultrathin structure possess higher valence band (VB) energy than that of

nanofibers with larger particle size (Weng et al., 2014). After forming homojunctions between BFO NFs and BFO nanoflakes, the staggered band potentials would introduce a new internal electrical field to provide a driving force to reduce the charge transfer barrier. The formed homojunction can promote the transfer of photogenerated holes (h<sup>+</sup>) from the VB of BFO NFs to the VB of BFO nanoflakes, whereas photogenerated electrons (e<sup>-</sup>) from the conduction band (CB) of BFO nanoflakes to that of BFO NFs. (2) SPR effect of Au NPs. The enhanced local electric field in the near-surface region of BFO induced by the SPR effect of Au NPs results in the further separation of photogenerated electrons and holes. The photogenerated electrons are thermodynamically favorable to transfer from the CB of BFO to Au NPs due to the Fermi energy of Au NPs is more positive than the CB potential of BFO (Li S. et al., 2013). The formed Schottky junction at the interfaces can act as trapping centers for photogenerated electrons, contributing the accumulation of photogenerated electrons at the surface of Au NPs and preventing the recombination of photogenerated electron-hole pairs. (3) Defects. The presence of Fe<sup>2+</sup>/Fe<sup>3+</sup> pairs located below the CB of BFO can act as electron/hole trapping centers and thus reduce the recombination rate (Zhang et al., 2014; Verma and Kotnala, 2016). In addition, the oxygen vacancy can introduce the defect state energy level and effectively regulate the band structure, thus significantly improve the separation of photogenerated charge carriers (Zhang C. et al., 2016). Under the effect of these aspects, the photocatalytic activities are remarkably enhanced.

During the process of photocatalytic reaction, a few photogenerated electrons in the CB of BFO nanoflakes can



react with oxygen molecules adsorbed on the surface to form superoxide radicals ( $\bullet\text{O}_2^-$ ). The photogenerated electrons transferred to the Au NPs can react with  $\text{Fe}^{2+}/\text{Fe}^{3+}$  pairs and oxygen vacancy defects. Meanwhile, a little part of photogenerated holes in the VB of BFO NFs can oxidize the absorbed  $\text{OH}^-$  and  $\text{H}_2\text{O}$  to hydroxyl radicals ( $\bullet\text{OH}$ ) (Dong et al., 2016; Hu et al., 2017). Finally, the photogenerated holes transferred the VB of BFO nanoflakes as well as the formed  $\bullet\text{O}_2^-$  and  $\bullet\text{OH}$  species can oxidation decomposition of MB dye molecules.

## CONCLUSIONS

Novel Au-induced hierarchical nanofibers/nanoflakes structured BFO homojunction ( $\text{Au}_x\text{-BFO}$ ,  $x=0, 0.6, 1.2, 1.8, 2.4$  wt%) were *in situ* synthesized by a simple reduction method under the analogous hydrothermal environment. The deposited Au NPs were distributed uniformly on the surface of BFO sample. The formed BFO nanoflakes were vertically assembled on BFO nanofibers to form a hierarchical architecture. The photocatalytic results showed that  $\text{Au}_{1.2}\text{-BFO}$  NFs samples exhibited the best photocatalytic activity with the photocatalytic efficiency of 85.76% after irradiation of 3 h. The remarkable enhanced photocatalytic activity could be

mainly attributed to the hierarchical nanofibers/nanoflakes structured homojunction, the SPR effect of Au NPs, as well as the presence of defects ( $\text{Fe}^{2+}/\text{Fe}^{3+}$  pairs and oxygen vacancy). This work provided a novel method to design efficient homojunctions with multiple functions in solar energy utilization.

## AUTHOR CONTRIBUTIONS

YL synthesized  $\text{Au}_x\text{-BFO}$  NFs samples and analyzed part of characterizations. JL is the supervisor of this research work. LC and HS helped writing. HZ analyzed Ferromagnetism measurements. HG and LF performed SEM, EDS, and TEM imaging and analyses. All authors have contributed to preparing the review article.

## FUNDING

This work was supported by the National Natural Science Foundation of China (Grant No. 51702189), the Shandong Provincial Natural Science Foundation, China (Grant No. ZR2017BEM033), and Science & Technology Plan of the Education Department of Shandong Province (grant No. J18KA002).

## REFERENCES

- Ahmada, S., Khanb, M. A., Sarfraz, M., Rehmana, A. U., Farooqwarisa, M., and Shakirc, I. (2017). The impact of Yb and Co on structural, magnetic, electrical and photocatalytic behavior of nanocrystalline multiferroic BiFeO<sub>3</sub> particles. *Ceram. Int.* 43, 16880–16887. doi: 10.1016/j.ceramint.2017.09.088
- Bharathkumar, S., Sakar, M., and Balakumar, S. (2016). Experimental evidence for the carrier transportation enhanced visible light driven photocatalytic process in bismuth ferrite (BiFeO<sub>3</sub>) one-dimensional fiber nanostructures. *J. Phys. Chem. C* 120, 18811–18821. doi: 10.1021/acs.jpcc.6b04344
- Chauhan, S., Kumar, M., Chhoker, S., Katyal, S. C., Singh, H., Jewariya, M., et al. (2012). Multiferroic, magnetoelectric and optical properties of Mn doped BiFeO<sub>3</sub> nanoparticles. *Solid State Commun.* 152, 525–529. doi: 10.1016/j.ssc.2011.12.037
- Chen, D., Niu, F., Qin, L., Wang, S., Zhang, N., and Huang, Y. (2017). Defective BiFeO<sub>3</sub> with surface oxygen vacancies: Facile synthesis and mechanism insight into photocatalytic performance. *Sol. Energ. Mat. Sol. C* 171, 24–32. doi: 10.1016/j.solmat.2017.06.021
- Chen, L., Meng, D., Wu, X., Wang, A., Wang, J., Wang, Y., et al. (2016). *In situ* synthesis of V<sup>4+</sup> and Ce<sup>3+</sup> self-doped BiVO<sub>4</sub>/CeO<sub>2</sub> heterostructured nanocomposites with high surface areas and enhanced visible-light photocatalytic activity. *J. Phys. Chem. C* 120, 18548–18559. doi: 10.1021/acs.jpcc.6b04131
- Chiu, Y. H., Chang, K. D., and Hsu, Y. J. (2018). Plasmon-mediated charge dynamics and photoactivity enhancement for Au-decorated ZnO nanocrystals. *J. Mater. Chem. A* 6, 4286–4296. doi: 10.1039/c7ta08543e
- Dong, F., Li, P., Zhong, J., Liu, X., Zhang, Y., Cen, W., et al. (2016). Simultaneous Pd<sup>2+</sup> doping and Pd metal deposition on (BiO)<sub>2</sub>CO<sub>3</sub> microspheres for enhanced and stable visible light photocatalysis. *Appl. Catal. A Gen.* 510, 161–170. doi: 10.1016/j.apcata.2015.11.022
- Dou, Y., Li, J., Cao, M., Su, D., Rehman, F., Zhang, J., et al. (2015). Oxidizing annealing effects on VO<sub>2</sub> films with different microstructures. *Appl. Surf. Sci.* 345, 232–237. doi: 10.1016/j.apsusc.2015.03.044
- Guo, Y., Li, J., Gao, Z., Zhu, X., Liu, Y., Wei, Z., et al. (2016). A simple and effective method for fabricating novel p-n heterojunction photocatalyst g-C<sub>3</sub>N<sub>4</sub>/Bi<sub>4</sub>Ti<sub>3</sub>O<sub>12</sub> and its photocatalytic performances. *Appl. Catal. B Environ.* 192, 57–71. doi: 10.1016/j.apcatb.2016.03.054
- Hu, X., Li, Y., Tian, J., Yang, H., and Cui, H. (2017). Highly efficient full solar spectrum (UV-vis-NIR) photocatalytic performance of Ag<sub>2</sub>S quantum dot/TiO<sub>2</sub> nanobelt heterostructures. *J. Ind. Eng. Chem.* 45, 189–196. doi: 10.1016/j.jiec.2016.09.022
- Huang, H., Xiao, K., Du, X., and Zhang, Y. (2017). Vertically aligned nanosheets-array-like BiOI homojunction: three-in-one promoting photocatalytic oxidation and reduction abilities. *ACS Sustain. Chem. Eng.* 5, 5253–5264. doi: 10.1021/acssuschemeng.7b00599
- Humayun, M., Zada, A., Li, Z., Xie, M., Zhang, X., Qu, Y., et al. (2016). Enhanced visible-light activities of porous BiFeO<sub>3</sub> by coupling with nanocrystalline TiO<sub>2</sub> and mechanism. *Appl. Catal. B Environ.* 180, 219–226. doi: 10.1016/j.apcatb.2015.06.035
- Huo, Y., Miao, M., Zhang, Y., Zhu, J., and Li, H. (2011). Aerosol-spraying preparation of a mesoporous hollow spherical BiFeO<sub>3</sub> visible photocatalyst with enhanced activity and durability. *Chem. Commun.* 47, 2089–2091. doi: 10.1039/c0cc04247a
- Irfan, S., Li, L., Saleemi, A. S., and Nan, C. (2017). Enhanced photocatalytic activity of La<sup>3+</sup> and Se<sup>4+</sup> co-doped bismuth ferrite nanostructures. *J. Mater. Chem. A* 5, 11143–11151. doi: 10.1039/c7ta01847a
- Ji, S., Dong, G., Luo, J., Ma, F., and Wang, C. (2018). Improved photocatalytic NO removal activity of SrTiO<sub>3</sub> by using SrCO<sub>3</sub> as a new co-catalyst. *Appl. Catal. B Environ.* 227, 24–34. doi: 10.1016/j.apcatb.2018.01.020
- Jovic, V., Chen, W., Sun-Waterhouse, D. X., Blackford, M. G., Idriss, H., and Waterhouse, G. I. N. (2013). Effect of gold loading and TiO<sub>2</sub> support composition on the activity of Au/TiO<sub>2</sub> photocatalysts for H<sub>2</sub> production from ethanol-water mixtures. *J. Catal.* 305, 307–317. doi: 10.1016/j.jcat.2013.05.031
- Li, Q., Hao, X., Guo, X., Dong, F., and Zhang, Y. (2015). Controlled deposition of Au on (BiO)<sub>2</sub>CO<sub>3</sub> microspheres: the size and content of Au nanoparticles matter. *Dalton Trans.* 44, 8805–8811. doi: 10.1039/c5dt00844a
- Li, S., Zhang, J., Kibria, M. G., Mi, Z., Chaker, M., Ma, D., et al. (2013). Remarkably enhanced photocatalytic activity of laser ablated Au nanoparticle decorated

- BiFeO<sub>3</sub> nanowires under visible-light. *Chem. Commun.* 49, 5856–5858. doi: 10.1039/c3cc40363g
- Li, Z., Shen, Y., Yang, C., Lei, Y., Guan, Y., Lin, Y., et al. (2013). Significant enhancement in the visible light photocatalytic properties of BiFeO<sub>3</sub>-graphene nanohybrids. *J. Mater. Chem. A* 1, 823–829. doi: 10.1039/c2ta00141a
- Lin, F., Shao, B., Li, Z., Zhang, J., Wang, H., Zhang, S., et al. (2017). Visible light photocatalysis over solid acid: enhanced by gold plasmonic effect. *Appl. Catal. B: Environ.* 218, 480–487. doi: 10.1016/j.apcatb.2017.06.076
- Modak, P., Lahiri, D., and Sharma, S. M. (2016). Correlation between structure and ferromagnetism in Nano-BiFeO<sub>3</sub>. *J. Phys. Chem. C* 120, 8411–8416. doi: 10.1021/acs.jpcc.6b02822
- Mohan, S., and Subramanian, B. (2013). A strategy to fabricate bismuth ferrite (BiFeO<sub>3</sub>) nanotubes from electrospun nanofibers and their solar light-driven photocatalytic properties. *RSC Adv.* 3, 23737–23744. doi: 10.1039/c3ra44085k
- Mudunkotuwa, I. A., and Grassian, V. H. (2010). Citric acid adsorption on TiO<sub>2</sub> nanoparticles in aqueous suspensions at acidic and circumneutral pH: surface coverage, surface speciation, and its impact on nanoparticle-nanoparticle interactions. *J. Am. Chem. Soc.* 132, 14986–14994. doi: 10.1021/ja106091q
- Nealon, G. L., Donnio, B., Greget, R., Kappler, J. P., Terazzi, E., and Gallani, J. L. (2012). Magnetism in gold nanoparticles. *Nanoscale* 4, 5244–5258. doi: 10.1039/c2nr30640a
- Niu, F., Chen, D., Qin, L., Gao, T., Zhang, N., Wang, S., et al. (2015). Synthesis of Pt/BiFeO<sub>3</sub> heterostructured photocatalysts for highly efficient visible-light photocatalytic performances. *Sol. Energ. Mat. Sol. C.* 143, 386–396. doi: 10.1016/j.solmat.2015.07.008
- Papadas, I., Christodoulides, J. A., Kioseoglou, G., and Armatas, G. S. (2015). A high surface area ordered mesoporous BiFeO<sub>3</sub> semiconductor with efficient water oxidation activity. *J. Mater. Chem. A* 3, 1587–1593. doi: 10.1039/c4ta05272b
- Qiao, Z., Yan, T., Li, W., and Huang, B. (2017). *In situ* anion exchange synthesis of In<sub>2</sub>S<sub>3</sub>/In(OH)<sub>3</sub> heterostructures for efficient photocatalytic degradation of MO under solar light. *New J. Chem.* 41, 3134–3142. doi: 10.1039/c6nj04119a
- Sakar, M., Balakumar, S., Saravanan, P., and Jaisankar, S. N. (2013). Annealing temperature mediated physical properties of bismuth ferrite (BiFeO<sub>3</sub>) nanostructures synthesized by a novel wet chemical method. *Mater. Res. Bull.* 48, 2878–2885. doi: 10.1016/j.materresbull.2013.04.008
- Sakar, M., Balakumar, S., Saravanan, P., and Jaisankar, S. N. (2016). Electric field induced formation of one-dimensional bismuth ferrite (BiFeO<sub>3</sub>) nanostructures in electrospinning process. *Mater. Design* 94, 487–495. doi: 10.1016/j.matdes.2016.01.029
- Singh, N., Salam, Z., Subasri, A., Sivasankar, N., and Subramania, A. (2018). Development of porous TiO<sub>2</sub> nanofibers by solvasonication process for high performance quantum dot sensitized solar cell. *Sol. Energ. Mat. Sol. C.* 179, 417–426. doi: 10.1016/j.solmat.2018.01.042
- Srivastav, S. K., and Gajbhiye, N. S. (2012). Low temperature synthesis, structural, optical and magnetic properties of bismuth ferrite nanoparticles. *J. Am. Ceram. Soc.* 95, 3678–3682. doi: 10.1111/j.1551-2916.2012.05411.x
- Sun, X., Wu, J., Li, Q., Liu, Q., Qi, Y., You, L., et al. (2017). Fabrication of BiOIO<sub>3</sub> with induced oxygen vacancies for efficient separation of the electron-hole pairs. *Appl. Catal. B Environ.* 218, 80–90. doi: 10.1016/j.apcatb.2017.06.041
- Tang, L., Feng, C., Deng, Y., Zeng, G., Wang, J., Liu, Y., et al. (2018). Enhanced photocatalytic activity of ternary Ag/g-C<sub>3</sub>N<sub>4</sub>/NaTaO<sub>3</sub> photocatalysts under wide spectrum light radiation: the high potential band protection mechanism. *Appl. Catal. B Environ.* 230, 102–114. doi: 10.1016/j.apcatb.2018.02.031
- Verma, K. C., and Kotnala, R. K. (2016). Tailoring the multiferroic behavior in BiFeO<sub>3</sub> nanostructures by Pb doping. *RSC Adv.* 6, 57727–57738. doi: 10.1039/C6RA12949H
- Villa, A., Dimitratos, N., Chan-Thaw, C. E., Hammond, C., Veith, G. M., Wang, D., et al. (2016). Characterisation of gold catalysts. *Chem. Soc. Rev.* 45, 4953–4994. doi: 10.1039/c5cs00350d
- Wang, B., Wang, S., Gong, L., and Zhou, Z. (2012). Structural, magnetic and photocatalytic properties of Sr<sup>2+</sup>-doped BiFeO<sub>3</sub> nanoparticles based on an ultrasonic irradiation assisted self-combustion method. *Ceram. Int.* 38, 6643–6649. doi: 10.1016/j.ceramint.2012.05.051
- Wang, H., Liang, L., Cheng, X., Luo, Y., and Sun, S. (2017). Facile fabrication of porous ZnS and ZnO films by coaxial electrospinning for highly efficient photodegradation of organic dyes. *Photochem. Photobiol.* 94, 17–26. doi: 10.1111/php.12836
- Wang, P., Lin, Z., Su, X., and Tang, Z. (2017). Application of Au based nanomaterials in analytical science. *Nano Today* 12, 64–97. doi: 10.1016/j.nantod.2016.12.009
- Wang, W., Li, N., Chi, Y., Li, Y., Yan, W., Li, X., et al. (2013). Electrospinning of magnetical bismuth ferrite nanofibers with photocatalytic activity. *Ceram. Int.* 39, 3511–3518. doi: 10.1016/j.ceramint.2012.10.175
- Weng, S., Fang, Z., Wang, Z., Zheng, Z., Feng, W., and Liu, P. (2014). Construction of teethlike homojunction BiOCl (001) nanosheets by selective etching and its high photocatalytic activity. *ACS Appl. Mater. Inter.* 6, 18423–18428. doi: 10.1021/am5052526
- Wu, L., Sui, W., Dong, C., Zhang, C., and Jiang, C. (2016). One-dimensional BiFeO<sub>3</sub> nanotubes: preparation, characterization, improved magnetic behaviors, and prospects. *Appl. Surf. Sci.* 384, 368–375. doi: 10.1016/j.apsusc.2016.05.043
- Xu, H., Wang, H., Shen, Y., Lin, Y., and Nan, C. (2014). Photocatalytic and magnetic behaviors of BiFeO<sub>3</sub> thin films deposited on different substrates. *J. Appl. Phys.* 116, 174307. doi: 10.1063/1.4901066
- Xu, W., Zheng, C., Hua, H., Yang, Q., Chen, L., Xi, Y., et al. (2015). Synthesis and photoelectrochemical properties of CdWO<sub>4</sub> and Cds/CdWO<sub>4</sub> nanostructures. *Appl. Surf. Sci.* 327, 140–148. doi: 10.1016/j.apsusc.2014.11.156
- Yang, R., Sun, H., Li, J., and Li, Y. (2018). Structural, magnetic and photocatalytic properties of Sr<sup>2+</sup> doped BiFeO<sub>3</sub> nanofibres fabricated by electrospinning. *Ceram. Int.* 44, 14032–14035. doi: 10.1016/j.ceramint.2018.04.256
- Ye, B., Han, X., Yan, M., Zhang, H., Xi, F., Dong, X., et al. (2017). Fabrication of metal-free two dimensional/two dimensional homojunction photocatalyst using various carbon nitride nanosheets as building blocks. *J. Colloid Interf. Sci.* 507, 209–216. doi: 10.1016/j.jcis.2017.08.002
- Zhang, C., Li, Y., Chu, M., Rong, N., Xiao, P., and Zhang, Y. (2016). Hydrogen-treated BiFeO<sub>3</sub> nanoparticles with enhanced photoelectrochemical performance. *RSC Adv.* 6, 24760–24767. doi: 10.1039/c5ra23699a
- Zhang, H., Liu, W., Wu, P., Hai, X., Guo, M., Xi, X., et al. (2014). Novel behaviors of multiferroic properties in Na-doped BiFeO<sub>3</sub> nanoparticles. *Nanoscale* 6, 10831–10838. doi: 10.1039/c4nr02557a
- Zhang, Q., Sando, D., and Nagarajan, V. (2016). Chemical route derived bismuth ferrite thin films and nanomaterials. *J. Mater. Chem. C* 4, 4092–4124. doi: 10.1039/c6tc00243a
- Zhang, T., Shen, Y., Qiu, Y., Liu, Y., Xiong, R., Shi, J., et al. (2017). Facial synthesis and photoreaction mechanism of BiFeO<sub>3</sub>/Bi<sub>2</sub>Fe<sub>4</sub>O<sub>9</sub> heterojunction nanofibers. *ACS Sustain. Chem. Eng.* 5, 4630–4636. doi: 10.1021/acsschemeng.6b03138
- Zhang, X., Wang, B., Wang, X., Xiao, X., Dai, Z., Wu, W., et al. (2015). Preparation of M@BiFeO<sub>3</sub> nanocomposites (M = Ag, Au) bowl arrays with enhanced visible light photocatalytic activity. *J. Am. Ceram. Soc.* 98, 2255–2263. doi: 10.1111/jace.13543

**Conflict of Interest Statement:** The authors declare that the research was conducted in the absence of any commercial or financial relationships that could be construed as a potential conflict of interest.

Copyright © 2019 Li, Li, Chen, Sun, Zhang, Guo and Feng. This is an open-access article distributed under the terms of the Creative Commons Attribution License (CC BY). The use, distribution or reproduction in other forums is permitted, provided the original author(s) and the copyright owner(s) are credited and that the original publication in this journal is cited, in accordance with accepted academic practice. No use, distribution or reproduction is permitted which does not comply with these terms.